

Semionic resonating valence bond states

Mohsin Iqbal,¹ Didier Poilblanc,² and Norbert Schuch¹

¹*JARA Institute for Quantum Information, RWTH Aachen, 52056 Aachen, Germany*

²*Laboratoire de Physique Théorique, C.N.R.S. and Université de Toulouse, 31062 Toulouse, France*

The nature of the kagome Heisenberg antiferromagnet (HAFM) is under ongoing debate. While recent evidence points towards a \mathbb{Z}_2 topological spin liquid, the exact nature of the topological phase is still unclear. In this paper, we introduce semionic Resonating Valence Bond (RVB) states, this is, Resonating Valence Bond states which are in the \mathbb{Z}_2 ordered double-semion phase, and study them using Projected Entangled Pair States (PEPS). We investigate their physics and study their suitability as an ansatz for the HAFM, as compared to a conventional RVB state which is in the Toric Code \mathbb{Z}_2 topological phase. In particular, we find that a suitably optimized “semionic simplex RVB” outperforms the equally optimized conventional “simplex RVB” state, and that the entanglement spectrum (ES) of the semionic RVB behaves very differently from the ES of the conventional RVB, which suggests to use the ES to discriminate the two phases. Finally, we also discuss the possible relevance of space group symmetry breaking in valence bond wavefunctions with double-semion topological order.

I. INTRODUCTION

Strongly correlated quantum systems exhibit a wide range of exciting and unconventional physical phenomena. One such effect which has recently received much attention due to its exotic properties are topological spin liquids, which—despite strong antiferromagnetic interactions—do not order magnetically even at very low temperatures due to the presence of strong quantum fluctuations; at the same time, these systems order topologically, which gives e.g. rise to fractionalized excitations with anyonic statistics.¹ It is believed that such phases are realized in materials such as Herbertsmithite, which show no sign of magnetic ordering down to very low temperatures,^{2,3} and where indeed recently signatures of fractionalized excitations have been experimentally observed.⁴

From a theoretical point of view, a prime candidate model for a topological quantum spin liquid is the Heisenberg antiferromagnet (HAFM) on the kagome lattice, which is believed to provide a good approximation of the physics of Herbertsmithite. Understanding the low-temperature phase diagram of the kagome HAFM has proven notoriously difficult, with several different phases competing with each other; the currently most convincing data, obtained using DMRG,^{5,6} suggests that the ground state of the kagome HAFM is a gapped \mathbb{Z}_2 topological spin liquid, i.e., a spin liquid with a $\log(2)$ correction to the topological entropy.

Given the hardness of understanding the exact ground state of the kagome HAFM, in order to obtain a qualitative understanding of the physics of the kagome HAFM, variational wavefunctions have been considered which are constructed to capture the physics of the antiferromagnetic interactions. Resonating Valence Bond (RVB) states have been proposed as an ansatz for antiferromagnets,⁷ and have helped to understand the spin liquid nature of antiferromagnets e.g. on the square or kagome lattice; in particular, it has been found that the kagome RVB state is a \mathbb{Z}_2 topological spin liquid in the phase of

the Toric Code model.⁸ Combining this with the observation of \mathbb{Z}_2 topological order in the aforementioned numerical simulations, this suggests that the kagome HAFM is a spin liquid in the same phase as the Toric Code. However, there is another topological phase with a topological entropy $\log(2)$, corresponding to the so-called double semion model; and while these two phases can in principle be distinguished by their quasi-particle excitations, this has up to now not been achieved in DMRG calculations.

In this paper, we apply variational wavefunctions to better understand the topological nature of the kagome HAFM. To this end, we introduce *semionic RVB states*, this is, RVB states which are in the phase of the double semion model, and investigate their properties and their suitability as a variational ansatz for the kagome HAFM. We show that semionic RVB states are in the same phase as the double semion model, and that they do not exhibit magnetic ordering. While the energy of the semionic RVB as an ansatz for the kagome HAFM is not competitive with the conventional RVB, we find that a two-parameter generalization termed *semionic simplex RVB* has a variational energy which is even below the energy of the analogous family of conventional simplex RVB states. We then proceed to study the entanglement properties of the semionic RVB state, and find that its entanglement spectrum exhibits features which are clearly distinct from the entanglement spectrum of the conventional RVB state (in particular, the minimum in the dispersion is at different momentum), and which therefore might be useful to discriminate the two \mathbb{Z}_2 topological phases e.g. in DMRG simulations. An interesting property of our wavefunction is that it explicitly breaks translational symmetry. While this might be an artefact of the construction, we find evidence that symmetry breaking is in fact energetically favorable, and we discuss possible consequences for the ground state of the kagome HAFM.

A central tool in our investigation are Projected Entangled Pair States (PEPS). PEPS allow for an exact description of a variety of states, in particular renormal-

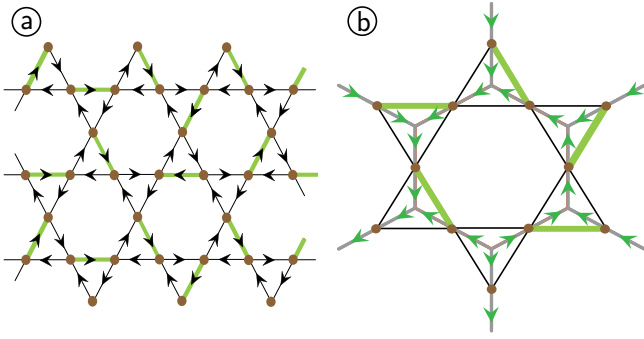


FIG. 1. (a) Dimer covering of the kagome lattice. The dimers are indicated in green, the arrows denote the canonical orientation of the singlets. (b) Arrow representation of dimer configuration. Each edge of the dual hexagonal lattice is assigned an orientation (arrow) which points into the triangle in which the dimer associated with the corresponding vertex of the kagome lattice lies.

ization fixed points of topological phases,^{9–11} but also Resonating Valence Bond states,⁹ where they have allowed for both analytical and high-precision numerical study of their properties.^{8,12} By combining elements of the PEPS constructions for the double semion model and the RVB state, we obtain a PEPS description of semionic RVB states, which we subsequently apply to study their physics.

This paper is structured as follows. In Sec. II, we introduce semionic RVB states through a mapping to loop models. In Sec. III, we show how to represent semionic RVB states as PEPS. Finally, in Sec. IV, we apply the PEPS representation of semionic RVBs to study their physics, including their generalization to semionic simplex RVBs in Sec. IV C.

II. SEMIONIC RVB STATES

In this section, we introduce semionic RVB states. To this end, consider the kagome lattice, Fig. 1. A *dimer covering* D of the kagome lattice is a covering of edges with *dimers*, such that every vertex is adjacent to exactly one dimer, as shown in Fig. 1a. We now place spin- $\frac{1}{2}$ particles at the vertices, and associate to every dimer covering D a state $|\sigma(D)\rangle = \bigotimes (|01\rangle - |10\rangle)$, where the singlets are placed on the dimers and oriented according to some convention (such as clock-wise around triangles). The (short-range) RVB state is then given as

$$|\psi_{\text{RVB}}\rangle = \sum_D |\sigma(D)\rangle.$$

Analogously, one can define a *dimer model* by replacing $|\sigma(D)\rangle$ by an orthonormal basis $|D\rangle$ of the space of dimer coverings D . Dimer models have been studied extensively, and it has in particular been shown that they exhibit \mathbb{Z}_2 topological order and appear as ground states

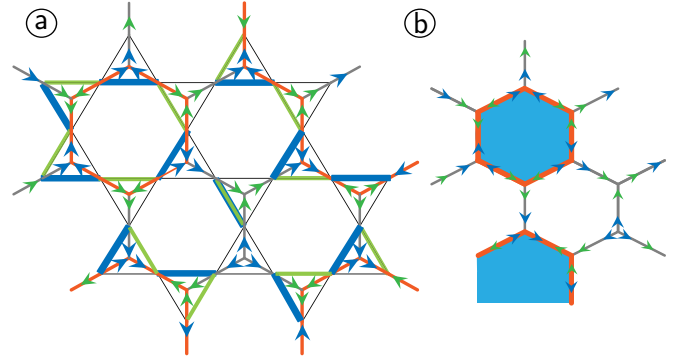


FIG. 2. (a) Mapping between dimer configurations and loop patterns. Given a reference dimer configuration (blue), any other dimer configuration (green) can be described by the arrows which need to be flipped in the corresponding arrow configuration (cf. Fig. 1b). Due to parity constraints, the edges with a flipped arrow form closed loops on the honeycomb lattice (red). (b) Loop patterns can be equivalently described by assigning binary variables (“colors”) to the plaquettes, and putting strings between different colors.

of local Hamiltonians which are locally equivalent to the Toric Code model;^{13–15} more recently, the same could be shown for RVB states.^{8,16,17}

Dimer coverings of the kagome lattice are in one-to-one correspondence to loop patterns on the hexagonal lattice. This can be shown using the “arrow representation” introduced by Elser and Zeng.¹⁸ To this end, consider the honeycomb lattice dual to the kagome lattice, cf. Fig. 1b. On every vertex of the kagome lattice (this is, every edge of the hexagonal lattice), we now place an arrow which points into the triangle in which the dimer adjacent to this vertex lies, as shown in Fig. 1b. By construction, the number of arrows pointing into any given triangle must be odd. We now fix a “reference dimer configuration” R , corresponding to a “reference arrow orientation”. Any other dimer configuration D is now characterized by the arrows which need to be flipped as compared to the reference arrow orientation. Due to parity constraints, the number of flipped arrows in each triangle must be even. Thus, by marking the edges of the kagome lattice corresponding to flipped arrows, we obtain a pattern of closed loops on the hexagonal lattice, which we denote by L_D ; vice versa, every loop pattern L has a dimer configuration D_L associated with it. The construction is illustrated in Fig. 2a. Note that the mapping between loop patterns and dimer configurations is only defined relative to the reference configuration, changing to a different reference configuration R' corresponds to flipping the link variables of the loop model according to the loop pattern $L_{R'}$.

The mapping between dimer configurations and loop patterns can be extended to quantum states: The dimer model $\sum_D |D\rangle$ is then mapped to the state $\sum_L |L\rangle$, a uniform superposition of all loop patterns on the hexagonal lattice; here, the state $|L\rangle$ consists of two-level systems which live on the edges, where the state $|1\rangle$ ($|0\rangle$)

marks the presence (absence) of a string. The latter is the ground state of the seminal Toric Code model by Kitaev, which has \mathbb{Z}_2 topological order.¹⁹ Given a suitable local encoding of $|D\rangle$, this mapping corresponds to a constant-depth unitary local circuit, and thus, the kagome dimer model is in the same phase as the toric code.

We can now use this mapping to construct resonating valence bond states and dimer models with semionic statistics. To this end, consider the state

$$|\psi_{\text{sem}}\rangle = \sum_L (-1)^{n(L)} |L\rangle,$$

where $n(L)$ is the number of closed loops in L . It describes the ground state of the double semion model, which also has \mathbb{Z}_2 topological order, but differs from the Toric Code model in the statistics of its excitations.²⁰ We are now ready to define the wavefunction of the *semionic dimer model*²¹

$$|\psi_{\text{sem-dimer}}\rangle = \sum_D (-1)^{n(L_D)} |D\rangle. \quad (1)$$

Again, given a suitable encoding of $|D\rangle$, it is locally equivalent to $|\psi_{\text{sem}}\rangle$ and thus in the same phase as the double semion model. In the same way, we also define the *semionic RVB state* as

$$|\psi_{\text{semRVB}}\rangle = \sum_D (-1)^{n(L_D)} |\sigma(D)\rangle. \quad (2)$$

Let us point out that fixing a reference configuration necessarily breaks the symmetry of the kagome lattice. As we will see, this gives rise to symmetry breaking in the semionic dimer and RVB model, while this is not the case for the conventional dimer/RVB state. This can be understood from the fact that changing the reference configuration corresponds to flipping a certain loop pattern: While this is a 1-to-1 mapping on the set of all loop configurations and thus does not affect the conventional dimer and RVB model, it changes the number of loops and thus the phases in the semionic wavefunctions.

III. PEPS REPRESENTATION

In this section, we show how semionic RVB states can be expressed using Tensor Networks.

A. Tensor Network for the semionic RVB state

Let us start by reviewing the tensor network representations of the Toric Code^{9,22} and of the double semion model.¹¹ Both models are superpositions of closed loops on the hexagonal lattice, though with different sign patterns. Any loop configuration has a dual representation in terms of Ising variables (i.e., two-level systems) on the plaquettes, where we put a loop whenever the plaquette

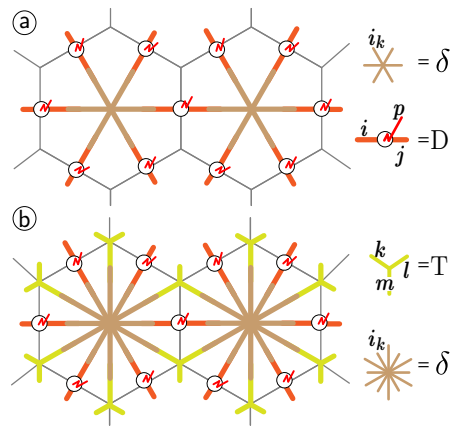


FIG. 3. Tensor network representation for (a) the Toric Code and (b) the double semion model.

variable changes, as illustrated in Fig. 2b; we will refer to these as “color” variables in the following. Note that the mapping from the color representation to loops is 2-to-1, since flipping all colors yields the same loop pattern.

In terms of these color variables, a tensor network representation of the Toric Code state can be obtained as follows: First, associate a 6-index Kronecker delta tensor δ_{i_1,\dots,i_6} ($i_k = 0, 1$, $\delta_{i_1,\dots,i_6} = 1$ iff all i_k are equal) to each plaquette; it carries the plaquette color. Second, associate a tensor

$$D_{i,j}^p = \delta_{i \oplus j, p} \quad (3)$$

which is 1 iff $i \oplus j = p$ to each edge (where \oplus denotes addition modulo 2). We now contract the i and j index of D with the indices of the δ tensors of the adjacent plaquettes, while p describes the physical index and remains uncontracted, as indicated in Fig. 3a. Since by Eq. (3) p is the difference of the adjacent plaquette color variables, this exactly yields the desired sum over all loop patterns.

In order to obtain a tensor network description of the double semion model, we additionally need to weigh each loop with -1 . Following Ref. 11, this is achieved by integrating the curvature of each loop by assigning a phase of $+i$ ($-i$) to each vertex with exactly one (two) adjacent black plaquettes, giving a phase of $(\pm i)^6 = -1$ for each closed loop. In terms of tensor networks, this is achieved by changing the δ tensor inside the plaquettes to a 12-index δ tensor, where the additional indices are contracted with tensors

$$T_{klm} = \begin{cases} +i & \text{if } k + l + m = 1 \\ -i & \text{if } k + l + m = 2 \\ 1 & \text{else} \end{cases}$$

placed on the vertices, as shown in Fig. 3b.

We are now in the position to construct the PEPS representation for the conventional and semionic RVB state. To this end, we start from the tensor network representation of the Toric Code or double semion model, respectively, and place a tripartite tensor E_{uvw} ($u, v, w =$

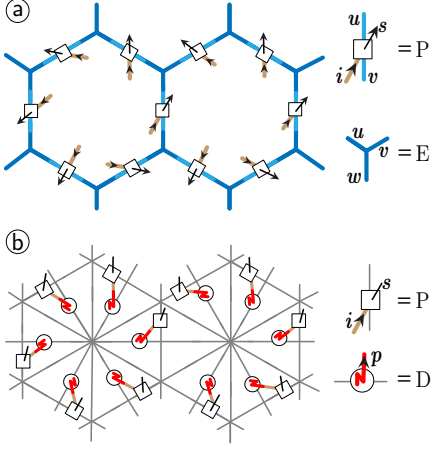


FIG. 4. Tensor network representation of the semionic RVB state. The tensor network in panel (a) needs to be combined with the tensor network for the double semion model (Fig. 3b), yielding a tensor network with the structure indicated in panel (b).

$0, 1, 2$), at each vertex of the honeycomb lattice, with one degree of freedom associated to each edge (i.e., the vertices of the kagome lattice). E is of the form

$$E_{uvw} = \begin{cases} 1 & u = v = w = 2 \\ \varepsilon_{uvw} & \text{otherwise} \end{cases} \quad (4)$$

with ε_{uvw} the fully antisymmetric tensor. E thus describes a triangle with either one singlet in the $\{0, 1\}$ subspace or with no singlet at all, where the absence of a singlet is indicated by a 2. Note that depending on the chosen orientation of the singlets, the signs in ε_{uvw} might have to be modified. At each site, we then add a tensor $P_{i;u,v}^s$ ($i = 0, 1$, $u, v = 0, 1, 2$, $s = 0, 1$) which picks a singlet from the E tensor of one of the adjacent triangles (and enforces the index of the other to be 2), as prescribed by the value of the loop and the reference configuration; this is,

$$P_{i;u,v}^s = \begin{cases} 1 & s = u, v = 2, i = 0 \\ 1 & s = v, u = 2, i = 1 \\ 0 & \text{otherwise} \end{cases}$$

where i is contracted with the “physical” index of the underlying loop model, s is the physical index of the RVB state, and u and v are contracted with the indices of the adjacent E ’s as prescribed by the reference configuration; the construction is illustrated in Fig. 4. Note that the tensor network can be simplified by grouping the tensors D and P into a single tensor.

Along the same line, we can also construct a tensor network representation of normal or semionic dimer models.⁸ To this end, we replace $P_{i;u,v}^s$ by $(P_{\perp})_{i;u,v}^{s,t} = P_{i;u,v}^s \delta_{i,t}$ ($t = 0, 1$) with physical indices s and t ; this is, the loop degree of freedom i remains physical and serves as an “indicator qubit” which allows to locally distinguish different singlet configurations; it is easy to see

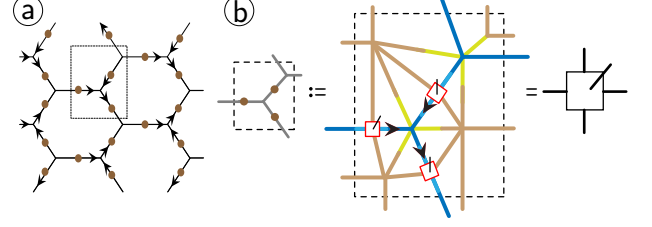


FIG. 5. (a) Blocking of the hexagonal and kagome lattice into square blocks. (b) Structure of the blocked tensor for the double semion model and semionic RVB state. For the double semion model, we can introduce the blue “string” indices which are redundant but ease the transition to the semionic RVB state.

that the resulting dimer model is locally unitarily equivalent to the corresponding loop model.²³ Following Ref. 8, we can generalize this to construct an interpolation from RVB states to dimer models, by using

$$P(\theta)_{i,u,v}^{s,t} = P_{i,u,v}^s w(\theta)_{i,t}, \quad (5)$$

where $w(\theta)_{i,t} = 1 + (-1)^{i+t}\theta$; here, $\theta = 1$ corresponds to the dimer model and $\theta = 0$ to the RVB state (with the t qubits in the $|+\rangle$ state).

B. Ground state manifold

In the preceding subsection, we have shown how to write the semionic RVB state as a PEPS. Yet, the double semion model is a topological model with a 4-fold degenerate ground space. In the following, we will show how to parametrize the ground space in terms of its PEPS representation.

We start by considering the PEPS representation of the double semion model; the generalization to the semionic RVB will be immediate. We first rewrite its PEPS representation by blocking three sites into a unit cell, thereby obtaining a square lattice, as indicated in Fig. 5a. (While the blocking is not required for the ground space parametrization, it will be useful for the numerical implementation.) For the blocked tensor, the δ tensor in each plaquette is decomposed as a contraction of four δ tensors, one for each block; overall, this results in a blocked tensor which has two indices at each side, one for each plaquette color (indicated by brown lines in Fig. 5b). In order to make the transition to the semionic RVB state easier, we add a third (redundant) index at each side, which is equal to the corresponding loop variable, i.e., the difference of the adjacent plaquette variables (the blue line in Fig. 5b; this index will later be replaced by the “singlet or 2” index of E). The auxiliary degrees of freedom of this new tensor have 16 non-zero values, which are illustrated in Fig. 6 with the corresponding amplitudes. These 16 configurations come in pairs which are related by flipping all plaquette colors, and thus correspond to the same physical state. It is now easy to see

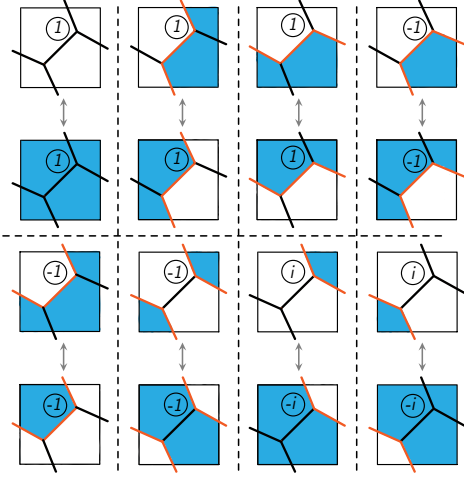


FIG. 6. Possible configurations of blocked tensor of the double semion model with the corresponding phases. The configurations form pairs (on top of each other) which are related by flipping the color, and thus have the same physical configuration, giving rise to a virtual \mathbb{Z}_4 symmetry (see text).

that this gives rise to a virtual symmetry of the tensor which corresponds to flipping all plaquette colors and in addition adjusting the phases depending on the loop configuration. This is, the tensor is invariant under a virtual symmetry action U_g on all four sides as shown in Fig. 7a. Here, $U_g = \zeta^g$ is a \mathbb{Z}_4 symmetry action, $g = \{0, 1, 2, 3\}$, with

$$\zeta = X \otimes \eta \otimes X, \quad (6)$$

where $X = \begin{pmatrix} 0 & 1 \\ 1 & 0 \end{pmatrix}$ acts on the color indices and $\eta = \begin{pmatrix} 1 & 0 \\ 0 & i \end{pmatrix}$ acts on the loop index.

The invariance of the PEPS tensor under this group action is closely related to topological order, and it can be used to parametrize different ground states.²² In particular, on a cylinder we can construct topologically distinct ground states by placing strings of U_g along the cylinder axis and projecting the left/right boundary condition of the cylinder onto irreducible representations of the group action, as shown in Fig. 7b. (Intuitively, this can be understood from the fact that using the symmetry of the tensor these strings can be freely moved through the lattice and thus should not affect the state locally.) This way, we obtain 16 possible states, which are labelled by a group element (flux) $\phi = 0, 1, 2, 3$ and an irreducible representation (charge) $c = 1, i, -1, -i$ of \mathbb{Z}_4 . Yet, the double semion model has only four distinct ground states, and there is indeed a redundancy in this description: As is discussed in Appendix A and as can also be checked numerically, eight of these states have norm zero, while the remaining eight form pairs which describe the same ground state; we thus find that the four ground states of the double semion model correspond to the following

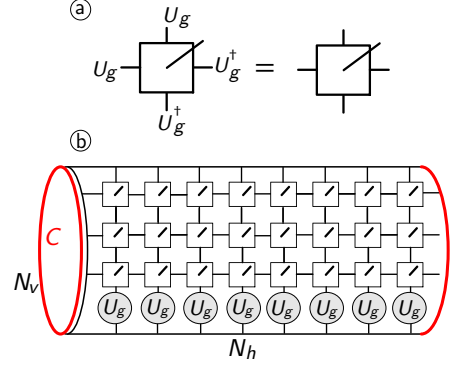


FIG. 7. (a) Virtual symmetry (G -invariance) of the PEPS tensor. (b) Parametrization of the ground state manifold in terms of the symmetry: The minimally entangled states are obtained by placing a “flux” string of group elements U_g along the horizontal closure, and projecting the boundary conditions onto irreducible representations (“charges”) of $U_g^{\otimes N_v}$.

flux and charge labels:

$$\begin{aligned} |\psi_1\rangle &\leftrightarrow (\phi = 0, c = 1) \quad \text{or} \quad (\phi = 2, c = -1) \\ |\psi_s\rangle &\leftrightarrow (\phi = 1, c = i) \quad \text{or} \quad (\phi = 3, c = -i) \\ |\psi_{\bar{s}}\rangle &\leftrightarrow (\phi = 1, c = -i) \quad \text{or} \quad (\phi = 3, c = i) \\ |\psi_b\rangle &\leftrightarrow (\phi = 0, c = -1) \quad \text{or} \quad (\phi = 2, c = 1) \end{aligned} \quad (7)$$

Here, we have labelled the ground states by the particle types of the model (the trivial particle, a conjugate pair of semions, and a boson); the identification can be e.g. understood by noting that the semionic ground states correspond to eigenstates of a loop operator of a bound state of an electric and a magnetic particle with charge/flux $\frac{1}{4}$ in a \mathbb{Z}_4 double model,¹⁹ which has semionic statistics.

In the case of semionic RVB states, the parametrization of the ground space is exactly analogous, with the only difference that η has to be replaced by $\eta = \text{diag}(1, 1, i)$ or $\eta = \text{diag}(i, i, 1)$, depending on whether $\{0, 1\}$ or 2 corresponds to the presence of a string in the double semion model, as determined by the reference configuration.

IV. RESULTS

In this section, we present a range of numerical results on semionic RVB states and extensions thereof, obtained using exact PEPS contraction techniques (see Appendix B for details).

A. Prerequisites

First, we need to fix a reference configuration of dimers. To this end, we choose a 6-site unit cell as indicated in Fig. 8a; this is the smallest unit cell for which reference configurations exist which allow to tile the lattice. We use

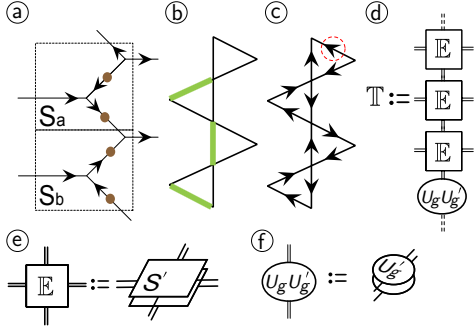


FIG. 8. (a) 6-site unit cell used for the numerical simulations. (b) Reference configuration used. (c) Energetically optimal singlet orientation for the semionic RVB. (d-f) Construction of the transfer operator (d), with the form of the individual ket-bra tensors and closures shown in (e) and (f), with S' the blocked tensor of panel (a).

the reference configuration shown in Fig. 8b; all other reference configurations are related to this configuration by a symmetry transformation of the lattice, cf. Appendix C.

We focus on the study of PEPS on infinite cylinders, see Fig. 7b, where we extrapolate in the cylinder circumference N_v . A central object in this study is the so-called transfer operator, which is obtained by contracting the ket and bra layer of the PEPS and considering one column, as shown in Fig. 8d-f. Such a transfer operator can be constructed for the overlap of two arbitrary ground states $|\psi_p\rangle$ and $|\psi_q\rangle$, and we denote it by \mathbb{T}_p^q . The largest eigenvalue γ_p^q of \mathbb{T}_p^q allows to determine the overlap $\langle\psi_q|\psi_p\rangle/(||\psi_p\rangle|||\psi_q\rangle) \sim (\hat{\gamma}_p^q)^{N_h}$ with $\hat{\gamma}_p^q = \gamma_p^q/(\gamma_p^p\gamma_q^q)^{1/2}$; in particular, if $\hat{\gamma}_p^q \rightarrow \text{const.} < 1$ as $N_v \rightarrow \infty$, $|\psi_p\rangle$ and $|\psi_q\rangle$ are orthogonal, whereas if $\hat{\gamma}_p^q = 1 + o(1/N_v)$, $|\psi_p\rangle$ and $|\psi_q\rangle$ describe the same state in the thermodynamic limit.²⁴ Note also that $-1/\log \hat{\gamma}_p^q$ relates to the “size” of the topological non-trivial excitations which couple ground states p and q . Also of interest are the second largest eigenvalues τ_p^q ; in particular, $\xi_p = -1/\log(\tau_p^p/\gamma_p^p)$ bounds the correlation length in the ground state $|\psi_p\rangle$.

B. Results for the semionic RVB state

In the following, we present our numerical results for the semionic RVB state. All results have been obtained with the reference configuration and with the singlet orientation shown in Fig. 8c; we have found this singlet orientation to be the (non-unique) one which minimizes the energy of the semionic RVB state as an ansatz for the kagome Heisenberg antiferromagnet.

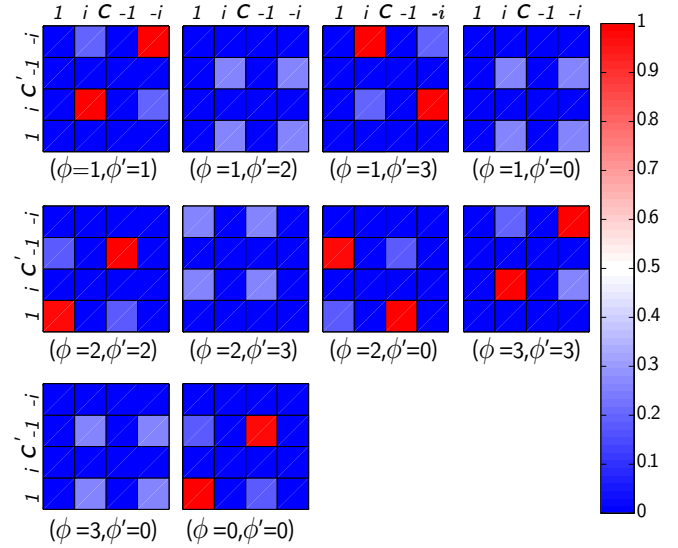


FIG. 9. Absolute value of the largest eigenvalues γ_p^q of the transfer operator \mathbb{T} , normalized to 1. ϕ (ϕ') and c (c') specify flux and charge in the ket (bra) layer of \mathbb{T} , i.e., $p \equiv (\phi, c)$ and $q \equiv (\phi', c')$. One can easily verify that only the four distinct states of Eq. (7) remain. Note that $(\gamma_p^q) = (\gamma_q^p)^*$.

1. Overlap of all sectors

To start with, we have considered the parametrization of the ground space in terms of fluxes and charges, as explained in Sec. IIIB. This parametrization gives a total of 16 states (corresponding to $\phi = 0, 1, 2, 3$ and $c = 1, i, -1, -i$), for which we show γ_p^q (normalized by $\max \gamma_p^q$) for all possible 16 values of p and q in Fig. 9. One can clearly see that eight of these states have zero norm, while the remaining eight form pairs for which $\gamma_p^q = (\gamma_p^p\gamma_q^q)^{1/2}$, thereby yielding the four ground states given in Eq. (7). On the other hand, for the remaining four states, $\gamma_p^q < (\gamma_p^p\gamma_q^q)^{1/2}$; this is, they indeed describe four distinct ground states of the resulting model.

2. Interpolation, phase, and correlations

Next, we have studied whether the semionic RVB state is in the same phase as the semionic dimer model (and thus the double semion model). To this end, we have used the interpolation $P(\theta)$ between the semionic RVB and the semionic dimer model given in Eq. (5). The results are shown in Fig. 10: We find that the largest eigenvalues γ_p^p for all four ground states remains equal (up to an splitting exponentially small in N_v , see inset), while γ_p^q for $p \neq q$ remains strictly smaller, which shows that the four ground states remain stable and orthogonal to each other. At the same time, the second largest eigenvalues remain bounded, ruling out a diverging correlation length. Together, this provides compelling evidence that the semionic RVB state is in the phase of the

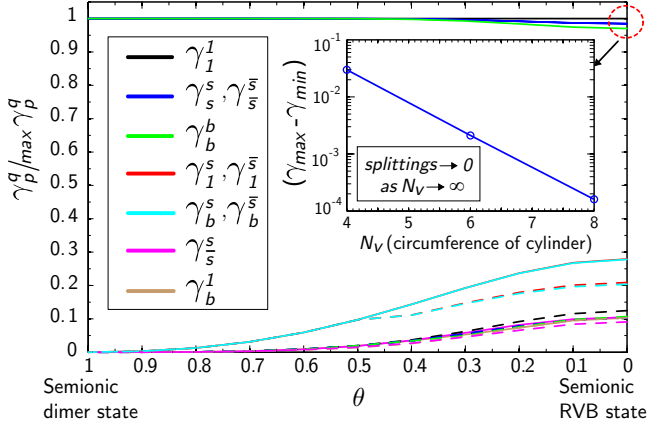


FIG. 10. Largest (solid lines) and second largest (dashed lines) eigenvalues for the different non-zero blocks of the transfer operator T_p^q along the interpolation from the semionic dimer state to the semionic RVB state for $N_v = 4$ (YC8 in the notation of Ref. 5). All $\gamma_p^q \rightarrow 1$ exponentially as $N_v \rightarrow \infty$ (inset), while the other eigenvalues stay bounded away, showing that the different topological ground states remain orthogonal and of equal norm, and the correlation length remains bounded, showing no sign of a phase transition (with $\xi \approx 0.42$ for the semionic RVB state), demonstrating that the semionic RVB state is in the phase of the double semion model.

double semion model. From this data, we can also extract the correlation length at the semionic RVB point, which we find to be $\xi \approx 0.42$, and the coherence length of topologically non-trivial semionic and bosonic excitations, $\xi_{\text{sem}} \approx 0.81$ and $\xi_{\text{bos}} \approx 0.44$. (For comparison, the values obtained for the RVB transfer operator²⁴ are $\xi \approx 0.79$, $\xi_{\text{spinon}} \approx 1.21$, and $\xi_{\text{vison}} \approx 0.79$.)

3. Ansatz for the kagome Heisenberg model

A main motivation for studying semionic RVB states was that they might form an alternative to the conventional RVB state as an ansatz for the ground state of the kagome Heisenberg antiferromagnet. We have thus computed the energy of the kagome AFM for all four ground states sectors and for different values of N_v ; the results are shown in Fig. 11. We find that the energies of the different ground states converge exponentially in N_v , as is expected for topologically degenerate ground states, with an extrapolated energy per site in the thermodynamic limit of $E_{\text{semRVB}} = -0.383(7)$. Fixing a reference configuration explicitly breaks translational invariance, leading to different energies for the different edges in a unit cell; the extent of translational symmetry breaking is shown in Fig. 12a, it is (approximately) identical for all topological sectors.

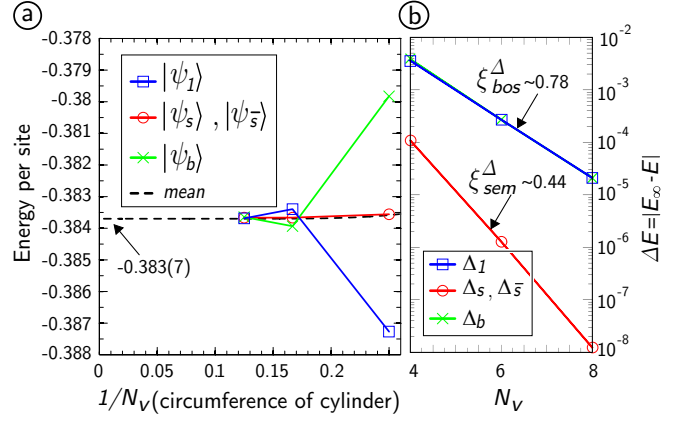


FIG. 11. (a) Energy per site for the semionic RVB state w.r.t. the Heisenberg Hamiltonian as a function of $1/N_v$ for the different topological sectors and $N_v = 4, 6, 8$; the extrapolated energy per site is $E_\infty = -0.383(7)$. (b) Exponentially vanishing finite-size difference between the energy per site and the extrapolated value for $N_v \rightarrow \infty$, with corresponding length scales $\xi_{\text{bos,sem}}^\Delta$.

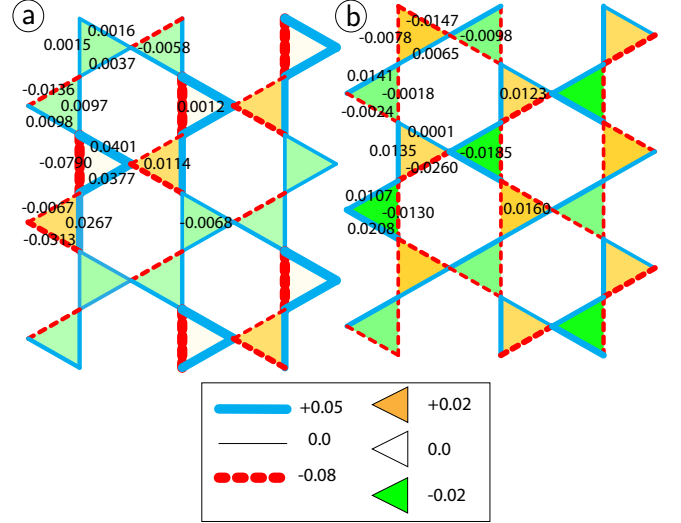


FIG. 12. Variations in the energy per link and the energy per triangle due to the explicit symmetry breaking induced by the choice of the reference configuration, for (a) the semionic RVB state with $N_v = 8$ and (b) the semionic simplex RVB state with $N_v = 6$. The thickness and color of each line indicates the magnitude and sign of the difference $\langle \mathbf{S}_i \cdot \mathbf{S}_j \rangle - E_{\text{semRVB}}^{(\text{simplex})}/2$; the intensity and color of each triangles indicates the deviation of the sum of bond energies from $\frac{3}{2} E_{\text{semRVB}}^{(\text{simplex})}$. The energies for the different topological sectors converge exponentially and break the symmetry in an identical way.

C. Semionic simplex RVB states

The energy $E_{\text{semRVB}} = -0.383(7)$ of the semionic RVB state as an ansatz for the Heisenberg antiferromagnet is higher than the energy found for the conventional RVB state,²⁵ $E_{\text{RVB}} = -0.3931$, which might suggest that the

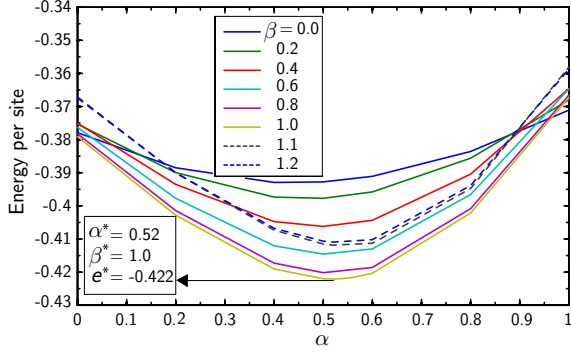


FIG. 13. Optimization for the simplex RVB: Energy per site as a function of the two parameters α and β for $N_v = 4$ (see text).

conventional RVB state is a more accurate description of the ground state of the kagome HAFM. On the other hand, it has been found in Ref. 26 that the energy of the RVB can be significantly improved by introducing only two extra parameters, an ansatz termed simplex RVB state. In the following, we study the same two-parameter family of semionic simplex RVB states, and find that by tuning these parameters, the family of semionic simplex RVB states achieves a variational energy even slightly below that of simplex RVB states.

1. Semionic simplex RVB ansatz

Let us first briefly sketch the idea of (semionic) simplex RVB states; for details, we refer the reader to Ref. 26. The construction is based on the observation that defect triangles, i.e., those without singlets, are energetically unfavorable. Zeng and Elser²⁷ showed that the energy can be significantly improved by allowing for singlets between next-nearest neighbors which are obtained by increasing the weight of the spin- $\frac{1}{2}$ subspace on each triangle. In the simplex RVB construction, a similar idea is used to improve the energy without increasing the bond dimension of the blocked tensors: First, the number of right-pointing defect triangles is reduced by changing E_{ijk} , Eq. (4), on the right-pointing triangles to E'_{ijk} with $E'_{222} = \beta < 1$ and $E'_{ijk} = E_{ijk}$ otherwise, and second, the energy of the left-pointing triangles is improved by multiplying the spins on each of those triangles by $\mathbb{1} - \alpha \mathbb{P}_{3/2}$, with $\mathbb{P}_{3/2}$ the projector onto the spin $3/2$ (i.e., permutationally invariant) subspace; since the right-pointing triangles sit inside the tensor, this does not increase the bond dimension D of the PEPS.

2. Ansatz for the kagome HAFM

Fig. 13 shows the energy for the HAFM Hamiltonian as a function of α and β . We find that for $N_v = 4$ the minimum is obtained for a value of $\alpha \approx 0.52$ and $\beta = 1$,

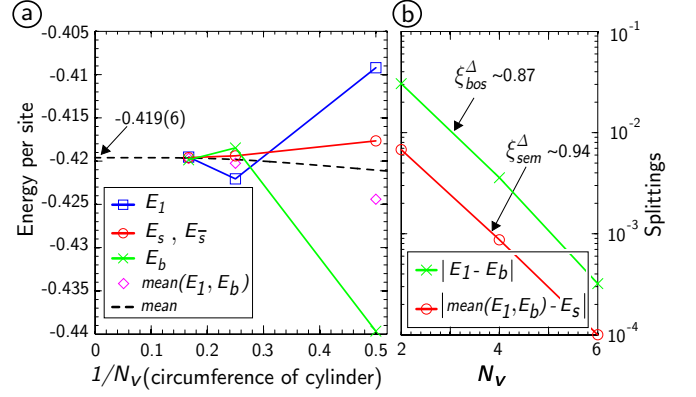


FIG. 14. Energy per site for the semionic simplex RVB state w.r.t. the Heisenberg Hamiltonian as a function of $1/N_v$ for the different topological sectors; the extrapolated energy per site is $E_\infty = -0.419(6)$. (b) Exponentially vanishing finite-size splitting for $N_v \rightarrow \infty$, with length scales $\xi_{\text{bos,sem}}^\Delta$.

and with the canonical singlet orientation of Fig. 1a, and we fix these values for the extrapolation in N_v . Fig. 14a shows the energy per site as a function of $1/N_v$ for the different topological sectors. The energies again converge exponentially in N_v (Fig. 14b), and we find the extrapolated energy to be $E_{\text{semRVB}}^{\text{simplex}} = -0.4196$, which is a significant improvement over the energy E_{semRVB} of the semionic RVB state, and in fact even slightly below the energy found for the conventional simplex RVB,²⁶ $E_{\text{RVB}}^{\text{simplex}} = -0.4181$.

Again, due to the choice of a reference pattern the system breaks the symmetries of the lattice. The variation in energy over the different bonds is shown in Fig. 12b, and we find that it is significantly reduced as compared to the unoptimized semionic RVB state; in fact, the observed variations in energy are comparable to those found in variational calculations for the kagome HAFM for certain choices of boundary conditions.^{5,6}

To better understand the nature of the symmetry breaking, we have also investigated the dependence between the variational energy and the degree of symmetry breaking within the two-parameter family of semionic simplex RVB. The results are shown in Fig. 15 for $N_v = 4$ and $N_v = 6$, where we plot the standard deviation of the energy over the different links (averaged over $|\psi_1\rangle$ and $|\psi_b\rangle$ for each link) vs. the variational energy. As one can see, there are strong finite-size effects. To be able to nevertheless single out the effects related to symmetry breaking in the thermodynamic limit, we additionally plot in the inset the difference between the energy per link for $|\psi_1\rangle$ and for $|\psi_b\rangle$ (averaged using the standard deviation) vs. the energy, which quantifies the finite size effects. We find that while for $N_v = 4$, the measured symmetry breaking is comparable to the finite-size effects, for $N_v = 6$ the finite size effects are significantly lower than observed symmetry breaking, which shows that the symmetry breaking will survive in the thermodynamic limit.

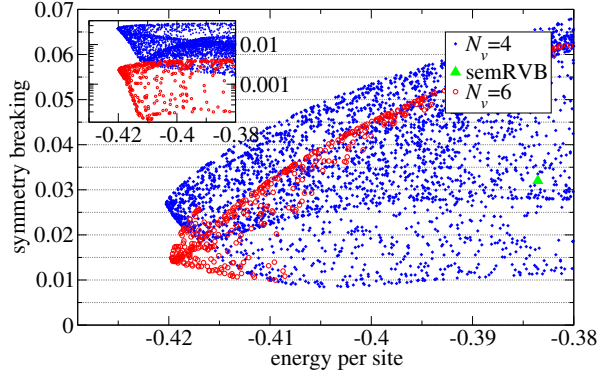


FIG. 15. Relation between symmetry breaking and variational energy for the semionic simplex RVB state for $N_v = 4$ and $N_v = 6$ (for randomly chosen values of α and β in a neighborhood of the optimum). The x axis shows the energy per site, and the y axis gives the standard deviation of the 12 inequivalent energies in the unit cell (averaged over $|\psi_1\rangle$ and $|\psi_b\rangle$). To be able to identify finite-size effects, we plot in the inset the standard deviation of the difference between the energy of $|\psi_1\rangle$ and $|\psi_b\rangle$ for each link, which measures the finite-size effects, vs. the energy. We find that for $N_v = 6$, the symmetry breaking is clearly above the finite size effects, suggesting it is favorable to break the symmetry to reach the optimal energy. The green triangle corresponds to the semionic RVB state.

We also find that the symmetry breaking at the energetic minimum is clearly larger than the minimal symmetry breaking compatible with the ansatz, which suggests that double-semion topological order in the kagome HAFM might favor symmetry breaking, though finite size effects cannot entirely be ruled out. (This should be contrasted with the behavior of the conventional simplex RVB, which we show in Appendix D.) Interestingly, we also found that the average energies in the left and right triangles are identical, despite the lattice symmetry breaking.

3. Interpolation, phase, and correlation length

Let us now study whether the optimized semionic simplex RVB is still in the phase of the double semion model. This is particularly important since the optimal value $\beta = 1$ corresponds to entirely ruling out defects on “right” triangles, which correspondingly rules out certain string configurations on the corresponding vertices of the honeycomb lattice. While one might think that this rules out certain loop patterns even on a global scale, one can easily verify that this is not the case as long as the reference configuration is different on the two “right” triangles in a unit cell (which is always the case).

In order to make sure that choosing $\beta = 1$ does not give rise to a phase transition, we therefore start by interpolating from the semionic dimer model to the point $\beta = 1$. The leading eigenvalues of the transfer operator along

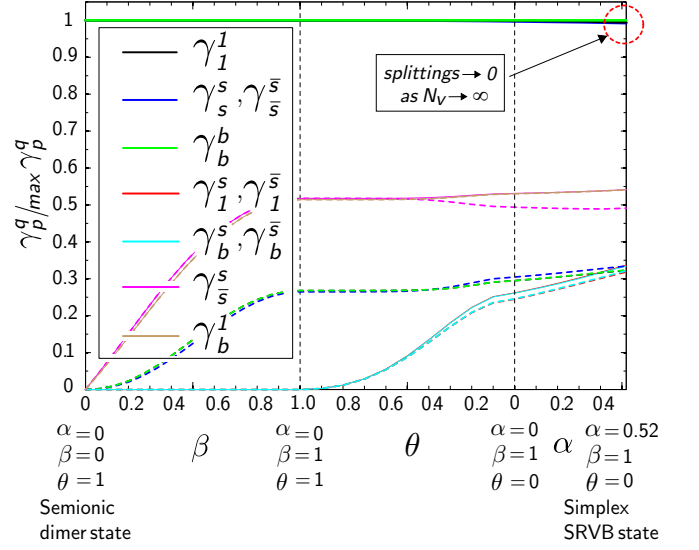


FIG. 16. Largest (solid lines) and second largest (dashed lines) eigenvalues for the different non-zero blocks of the transfer operator T_p^q along the interpolation from the semionic dimer state to the semionic simplex RVB state for $N_v = 6$ (YC12) where the interpolation is performed in three steps as indicated. As for the semionic RVB (Fig. 10), we find that the system stays topologically ordered with no sign of a phase transition and finite correlation length, showing that the semionic simplex RVB does not break spin rotation symmetry and is in the phase of the double semion model.

this interpolation are shown in the left part of Fig. 16: We find that the transfer operator remains gapped and thus the semionic dimer model with $\beta = 1$ is in the same phase as the original semionic dimer state, but exhibits an effective length scale of $-1/\log(0.5)$. Both these facts can be understood from a renormalization argument: By blocking a 1×2 unit cell given by the reference configuration and renormalizing the allowed loop configurations, one finds that all loop patterns can be obtained after one RG step, yet with different weights, giving rise to an effective length scale in the system.

We then continue to interpolate from the dimer state with $\beta = 1$ to the corresponding semionic RVB state using θ , Eq. (5) (middle part of Fig. 16), and finally increase α to its optimal value (note that the last interpolation is not defined for the dimer state). Along the whole interpolation, the spectrum of the transfer operator exhibits no sign of a phase transition—the correlation length is finite, and the different topological sectors remain orthogonal throughout. At the semionic simplex RVB point, we obtain a correlation length of $\xi \approx 0.90$ for topologically trivial and $\xi_{\text{sem}} \approx 0.91$ and $\xi_{\text{bos}} \approx 1.63$ for topologically non-trivial semionic and bosonic excitations, respectively; remarkably, the ordering of ξ_{bos} and ξ_{sem} has changed as compared to the semionic RVB state.

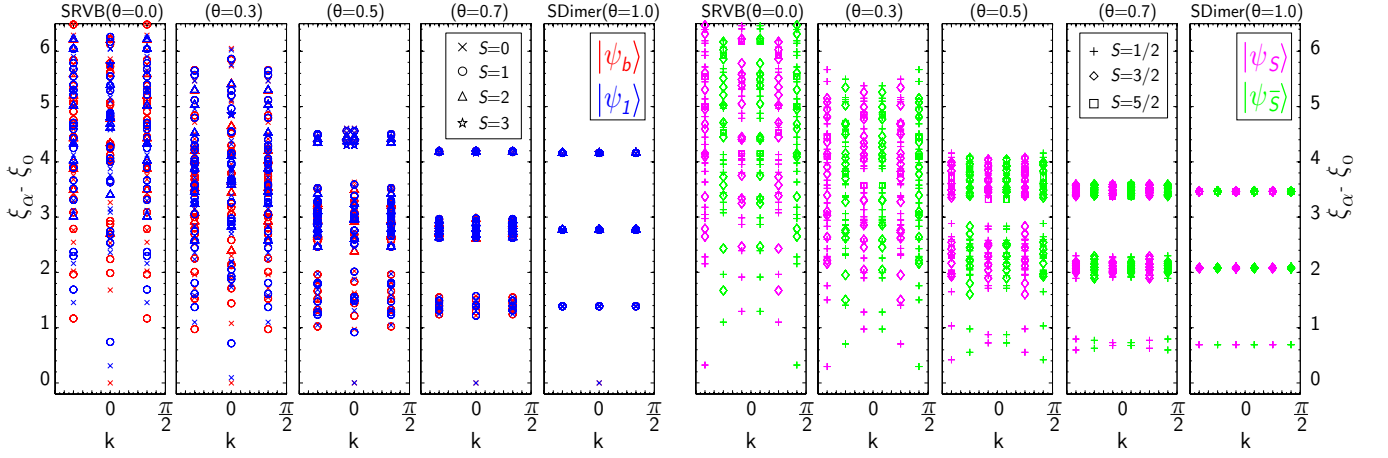


FIG. 17. Entanglement spectrum (ES) for the interpolation from the semionic dimer state ($\theta = 1$) to the semionic RVB state ($\theta = 0$) for an infinite cylinder with $N_v = 6$. The left (right) panel shows the integer (half-integer) spin sector of the ES, which correspond to the bosonic (semionic) ground states and are not coupled by the entanglement Hamiltonian. The momentum is restricted to $-\pi/2 \leq k \leq \pi/2$ due to the blocking of two unit cells (Fig. 8a).

D. Entanglement properties

An important way to characterize topologically ordered phases is via their entanglement properties. The exact description of (simplex) semionic RVB states in terms of PEPS allows to exactly compute their entanglement properties,²⁸ which we analyze in the following. The fits are w.r.t. the average over the four sectors.

1. Entanglement entropy

First, we have computed the (von Neumann) entanglement entropy^{29,30} of the semionic RVB and semionic simplex RVB for a bipartition of the minimally entangled states of Eq. (7) into two half-cylinders. The results are shown in Fig. 18. By fitting the entanglement as

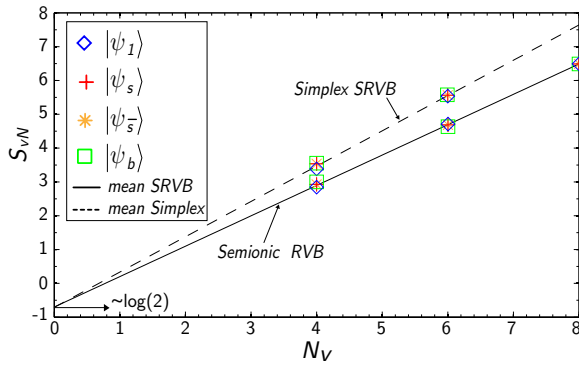


FIG. 18. Entanglement entropy S_{vN} for the semionic (solid line) and semionic simplex (dashed line) RVB state, where the fit is w.r.t. the average of the four topological sectors. In both cases, we find a topological correction of $\log(2)$, indicative of a \mathbb{Z}_2 topological phase.

$S_{vN} \sim cN_v - \gamma$, we find that both states exhibit a topological correction $\gamma \approx \log(2)$, in accordance with their \mathbb{Z}_2 topological nature.

2. Entanglement spectrum

We have also computed the entanglement spectrum using PEPS-based methods.²⁸ The results are shown in Fig. 17 separately for integer spin (bosonic ground states) and half-integer spin (semionic ground states) excitations, with k the momentum w.r.t. to a 3-site unit cell (Fig. 5b), where the 2×1 blocking due to the reference configuration (Fig. 8a,b) restricts k to the reduced Brillouin zone $k = -\pi/2 \dots \pi/2$; note that for the semionic sectors, k is shifted by $2\pi/(4N_v)$ due to the presence of a $1/4$ flux in the system. (In the PEPS representation, this is reflected in the fact that the translation operator is “dressed” with U_g , i.e., it translates and grows a string of U_g at the same time, cf. Fig. 7b, which gives rise to a corresponding shift in momentum.)

A remarkable feature which distinguishes the entanglement spectrum from the one obtained for the RVB state^{8,25} is that the (possibly gapless) minimum of the dispersion in the half-integer spin sector is at $k = \pm\pi/2$ rather than at $k = 0$; this might serve as an indicator to numerically distinguish the two phases.

V. CONCLUSIONS

In this paper, we have considered variational wavefunctions for kagome Heisenberg antiferromagnets (HAFMs). We have introduced semionic Resonating Valence Bond (RVB) states and semionic dimer models, which are constructed to be in the same phase as the double semion

model. We have discussed how to parametrize the ground state manifold of this model, and have subsequently used PEPS techniques based on the transfer operator to show that the semionic RVB state is indeed in the same phase as the double semion model. We have also verified that the semionic RVB state does not break spin $SU(2)$ symmetry; it does however explicitly break the symmetry of the lattice by construction. We have also computed the energy w.r.t. kagome HAFM and found it to be not competitive with the conventional RVB ansatz.

We have subsequently generalized semionic RVB states to semionic simplex RVB states, which use next-nearest neighbor singlets to decrease the energy of the ansatz. We have found that with this optimization, the energy of the semionic simplex RVB, $E_{\text{semRVB}}^{\text{simplex}} = -0.4196$, outperforms the energy of the conventional simplex RVB with the same optimization, while still being in the phase of the double semion model, leaving open the possibility that the topological order of the kagome HAFM is described by the double semion model.

We have also computed the entanglement properties of the semionic and semionic simplex RVB. We have found that both exhibit a \mathbb{Z}_2 correction to the topological entropy, and we have found that the entanglement spectrum of the semionic RVB exhibits features which clearly distinguish it from the entanglement spectrum of the conventional RVB state; in particular, while both seem to be gapless, the minimum of the dispersion is at $k = \frac{\pi}{2}$ for the semionic RVB, as opposed to $k = 0$ for the conventional RVB.

Let us finally comment on the breaking of lattice (space group) symmetry which naturally appears in the semionic RVB from the choice of a reference configuration. It is not clear yet whether such a discrete symmetry breaking is an essential feature of any RVB state with that kind of topological order or whether it is also possible to construct translation-invariant wavefunctions. In any case, the coexistence of so-called "Valence Bond

Crystal" (VBC) order and topological order might be relevant to the original kagome HAFM. Indeed, small bond modulations seem to be ubiquitous in DMRG simulations on finite clusters^{5,6} and whether those completely disappear in the thermodynamic limit is under debate. In addition, Lanczos exact diagonalization of an effective quantum dimer model provide evidence of competing VBC ground states³¹ including a 2×1 "columnar" VBC (CVBC) which possesses the same real-space structure as the semionic RVB constructed in this work. Note that a CVBC with coexisting double-semionic topological order would give a degeneracy of 96 (24 due to space-group symmetry breaking times 4 for topological order) of the ground state space in the thermodynamic limit. Interestingly, we expect that this degeneracy might not be completely lifted in finite systems, as the two semionic sectors should remain degenerate. Whether semionic VBC phases can be realized in generalized quantum dimer model³¹ is left for further studies.

Note added: During completion of this work, we learned that Qi, Gu, and Yao³² had independently introduced quantum dimer models with double-semion topological order in a way similar to ours, and studied their corresponding Hamiltonians and the nature of their excitations; and that Zaletel, Lu, and Vishvanath³³ have found general symmetry arguments which suggest that it is impossible to construct a translationally invariant double-semion state on the kagome lattice.

Acknowledgements

M.I. and N.S. acknowledge funding by the Alexander von Humboldt foundation, and computational resources provided by JARA-HPC via grants jara0084 and jara0092. D.P. acknowledges fundings by the "Agence Nationale de la Recherche" under grant No. ANR 2010 BLANC 0406-0.

Appendix A: Ground state parametrization

In this appendix, we briefly sketch how to show analytically that the parametrization of the ground states of the double semion model in terms of group elements and irreps of \mathbb{Z}_4 only gives rise to 4 distinct ground states, Eq. (7). All arguments work at the level of a single column, and are given for the loop model (since the RVB states constructed from it are always less distinguishable).

Let us first show that eight of the states vanish. To this end, consider a column of the PEPS, and consider the case where the flux (the horizontal string of U_ϕ in Fig. 7b) is trivial, $U_\phi = \mathbb{1}$, $\phi = 0$. This implies that the color index is not flipped when closing the bound-

ary with U_ϕ , and thus, the number of loops across any vertical cut (and thus in particular at the left and right boundary) is even. On the other hand, the irreps $c = \pm i$ are supported inside the subspace with an odd number of strings at the boundary [since every string acquires a phase i from η , Eq. (6)], and thus, the states with $\phi = 0$ and $c = \pm i$ vanish. The argument for the other states goes analogously.

Second, let us show why pairs of boundary conditions describe the same state. Again, consider the case with no flux, $U_\phi = \mathbb{1}$, $\phi = 0$. and with trivial irrep $c = 1$. Having $c = \pm 1$ is equivalent to a projection $P_\pm \otimes \Pi_{0 \bmod 4} + P_\mp \otimes \Pi_{2 \bmod 4}$, where P_+ (P_-) denotes the projection onto the subspace of states at one boundary which are invariant (change their sign) under flipping

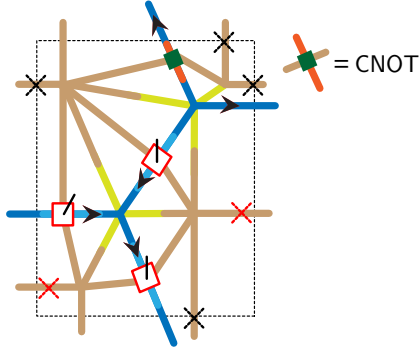


FIG. 19. Optimizations for the semionic RVB tensor network (see text).

of all colors, and $\Pi_{k \bmod 4}$ denotes the space of loop configurations with $k \bmod 4$ loops at the boundary. Now consider $c = 1$ and start with a column with no loops at all: Flipping all colors at one side gives rise to a closed loop around the column, which leads to no sign change. For $c = -1$, the same procedure flips the overall sign, which can however be compensated by a U_ϕ closure, $\phi = 2$, on a vertical bond, which corresponds to a Z on the loop index and thus exactly undoes the sign change, thus leaving the state invariant. Starting from this empty loop configuration, we can now create any other loop configuration in the $c = \pm 1$ subspace by elementary moves, and it is straightforward to check that all of these give the same result whether $c = 1$ and $\phi = 0$ or $c = -1$ and $\phi = 2$. The argument for the other pairs goes again analogously.

Appendix B: Numerical implementation

For the numerical implementation, we have used exact diagonalization of the transfer operator using iterative eigensolvers and standard tensor network methods; in particular, the transfer operator, Fig. 8d, is applied to a vector by contracting one tensor \mathbb{E} after the other with the vector. However, the original tensor network still has a bond dimension $D = 2 \times 2 \times 3 = 12$. Thus, we first simplify the tensor network to reduce the bond dimension. The basic idea is to make use of the fact that we have a redundant description, as we have both a color variable and a link variable (encoded in the E tensors). Thus, we can reduce the number of bonds used for color variables, by re-computing the color variable every time a link is crossed. This is illustrated in Fig. 19: We start by removing all color indices which are marked with a black cross. The color information is still passed by one bond in horizontal and one in vertical direction, and is thus available in every tensor; the construction of the tensor network (namely, the combined D and P tensor) ensures that the color index is flipped every time it crosses a link. However, this is not true for the top right plaquette in the tensor; this is resolved by adding a “CNOT”

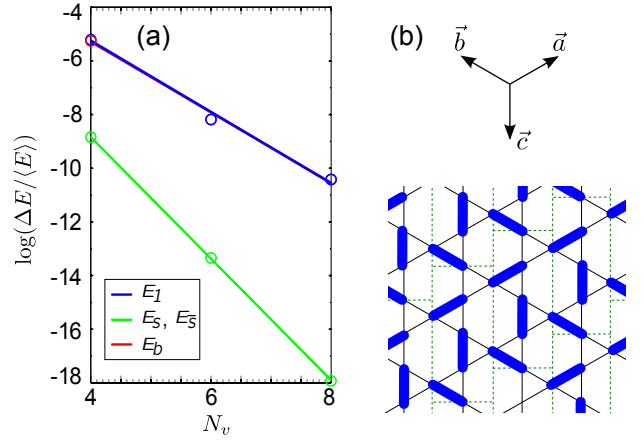


FIG. 20. (a) Energy difference between inequivalent reference configurations. The plot shows the difference of the average energy per bond between semionic RVBs with two inequivalent reference configurations as a function of N_v ; we find that the energies converge exponentially in N_v . (b) The reference configuration of Fig. 8b, with the blocking of Fig. 8a (indicated by green dotted lines). The blocking gives rise to columnar order along \vec{a} , which is left invariant by inversion, translation, and reflection about \vec{a} , where the last transformation is incompatible with the cylinder geometry.

tensor which enforces the plaquette colors to be equal or different depending on whether the link index is $\{0, 1\}$ or 2, relative to the reference configuration. A further improvement can be obtained by additionally removing the indices marked by a red cross in all the tensors but one in a column; the remaining tensor then passes the color index in the horizontal direction, while it is passed vertically within each column. This leads to a further reduction of the relevant horizontal bond dimension D_h (the memory requirement grows like $D_h^{2N_v}$). In a final step, we consider the ket-bra tensor \mathbb{E} (Fig. 8e) obtained from the optimized tensor in a 2×1 unit cell and further optimize the bond dimension using a singular value decomposition.

Appendix C: Different reference configurations

In this appendix, we briefly discuss the dependence of the energies on the choice of reference configurations. In Sec. IV, we have fixed a 6-site unit cell, cf. Fig. 8a. Within this unit cell, we can choose 8 possible reference configurations (such as the one in Fig. 8b). We find numerically that they form two groups of 4 reference configurations each: For any reference configuration within each group, the variational energies are identical for any finite N_v (though with a different symmetry breaking pattern); on the other hand, reference configurations from different groups give different energies, which however converge to the same value in the thermodynamic limit $N_v \rightarrow \infty$ as shown in Fig. 20a for the HAFM Hamiltonian. As we explain in the following, this

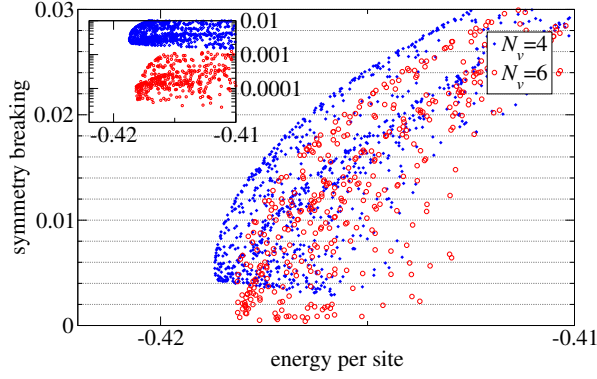


FIG. 21. Symmetry breaking and finite size effects (inset) vs. variational energy for the conventional simplex RVB, for randomly chosen α and β around the optimal value. The quantities plotted are the same as in Fig. 15.

can be understood from the symmetries of the infinite kagome lattice vs. the symmetries of the (YC) kagome lattice on a cylinder.

Given our choice of the 6-site unit cell, Fig. 8a, each reference configuration leads to a dimer covering of the kagome lattice with columnar order, illustrated in Fig. 20b for the reference configuration of Fig. 8b. Here, the dimers arrange in columns along the \vec{a} axis; indeed, one can easily see that the orientation of the columns originates from the choice of our 6-site unit cell. There are 3 symmetry transformations which preserve the columnar dimer order along \vec{a} : Inversion, translation, and reflection about the \vec{a} axis, giving rise to 8 different dimer configurations with columnar order along \vec{a} .

While inversion and translation respect the symmetry of the finite cylinder, and thus give rise to the same energy, reflection about the \vec{a} axis does not, which explains the different energies for finite N_v . On the other hand, it is of course a symmetry of the infinite lattice, which is why the energies converge for $N_v \rightarrow \infty$.

There are also two other possible orientations of the columnar order along \vec{b} or \vec{c} . Columnar order along \vec{b} is related to \vec{a} by a reflection about the \vec{c} axis, which respects the symmetry of the cylinder, and thus gives identical energies as before (though it corresponds to a shifted blocking of the PEPS as compared to Fig. 5a); thus, each of the energies belongs in fact to a set of 8 reference dimer coverings (4 along \vec{a} and 4 along \vec{b}). Columnar order along \vec{c} , on the other hand, is not related by a cylinder symmetry to the other cases and requires a horizontally oriented 6-site unit cell; it therefore gives rise to a third group of 8 equivalent reference dimer coverings which we expect to have a yet different energy for finite N_v , and to converge again to the same value for $N_v \rightarrow \infty$.

Appendix D: Symmetry breaking in the conventional simplex RVB state

In Fig. 21 we provide the data on symmetry breaking and finite size effects vs. variational energy for the conventional simplex RVB,²⁶ in analogy to Fig. 15. We see that both the symmetry breaking and finite size effects are much smaller than in the case of the semionic simplex RVB, suggesting that symmetry breaking vanishes in the thermodynamic limit.

- ¹ L. Balents, *Nature* **464**, 199 (2010).
- ² P. Mendels *et al.*, *Phys. Rev. Lett.* **98**, 077204 (2007).
- ³ J. S. Helton *et al.*, *Phys. Rev. Lett.* **98**, 107204 (2007).
- ⁴ T.-H. Han *et al.*, *Nature* **492**, 406 (2012).
- ⁵ S. Yan, D. A. Huse, and S. R. White, *Science* **332**, 1173 (2011), arXiv:1011.6114.
- ⁶ S. Depenbrock, I. P. McCulloch, and U. Schollwoeck, *Phys. Rev. Lett.* **109**, 067201 (2012), arXiv:1205.4858.
- ⁷ P. W. Anderson, *Mater. Res. Bull.* **8**, 153 (1973).
- ⁸ N. Schuch, D. Poilblanc, J. I. Cirac, and D. Pérez-García, *Phys. Rev. B* **86**, 115108 (2012), arXiv:1203.4816.
- ⁹ F. Verstraete, M. M. Wolf, D. Perez-García, and J. I. Cirac, *Phys. Rev. Lett.* **96**, 220601 (2006), quant-ph/0601075.
- ¹⁰ O. Buerchaper, M. Aguado, and G. Vidal, *Phys. Rev. B* **79**, 085119 (2009), arXiv:0809.2393.
- ¹¹ Z.-C. Gu, M. Levin, B. Swingle, and X.-G. Wen, *Phys. Rev. B* **79**, 085118 (2009), arXiv:0809.2821.
- ¹² L. Wang, D. Poilblanc, Z.-C. Gu, X.-G. Wen, and F. Verstraete, *Phys. Rev. Lett.* **111**, 037202 (2013), arXiv:1301.4492.
- ¹³ D. S. Rokhsar and S. A. Kivelson, *Phys. Rev. Lett.* **61**, 2376 (1988).
- ¹⁴ R. Moessner and S. L. Sondhi, *Phys. Rev. Lett.* **86**, 1881 (2001), cond-mat/0007378.
- ¹⁵ G. Misguich, D. Serban, and V. Pasquier, *Phys. Rev. Lett.* **89**, 137202 (2002), cond-mat/0204428.
- ¹⁶ A. Seidel, *Phys. Rev. B* **80**, 165131 (2009), arXiv:0906.0357.
- ¹⁷ Z. Zhou, J. Wildeboer, and A. Seidel, *Phys. Rev. B* **89**, 035123 (2014), arXiv:1310.8000.
- ¹⁸ V. Elser and C. Zeng, *Phys. Rev. B* **48**, 13647 (1993).
- ¹⁹ A. Kitaev, *Ann. Phys.* **303**, 2 (2003), quant-ph/9707021.
- ²⁰ M. Freedman, C. Nayak, K. Shtengel, K. Walker, and Z. Wang, *Ann. Phys.* **310**, 428 (2004), cond-mat/0307511.
- ²¹ There are two reasons to define semionic dimer models w.r.t. loop patterns on the honeycomb rather than on the kagome lattice. First, while overlap graphs of dimer configurations yield loop configurations also on the kagome lattice, this mapping is not surjective (i.e., relative to a given reference configuration, not every loop pattern corresponds to a dimer pattern), and second, counting the number of loops is ambiguous on non-trivalent lattices.
- ²² N. Schuch, I. Cirac, and D. Pérez-García, *Ann. Phys.* **325**, 2153 (2010), arXiv:1001.3807.
- ²³ This can be seen by adding a spin- $\frac{1}{2}$ state at every edge of the kagome lattice, and applying a unitary first on the up and then on the down triangles which creates singlets depending on the arrow pattern corresponding to the loop

- configuration.
- ²⁴ N. Schuch, D. Poilblanc, J. I. Cirac, and D. Perez-Garcia, Phys. Rev. Lett. **111**, 090501 (2013), arXiv:1210.5601.
 - ²⁵ D. Poilblanc, N. Schuch, D. Pérez-García, and J. I. Cirac, Phys. Rev. B **86**, 014404 (2012), arXiv:1202.0947.
 - ²⁶ D. Poilblanc and N. Schuch, Phys. Rev. B **87**, 140407 (2013), arXiv:1302.0306.
 - ²⁷ C. Zeng and V. Elser, Phys. Rev. B **42**, 8436 (1990).
 - ²⁸ J. I. Cirac, D. Poilblanc, N. Schuch, and F. Verstraete, Phys. Rev. B **83**, 245134 (2011), arXiv:1103.3427.
 - ²⁹ M. Levin and X.-G. Wen, Phys. Rev. Lett. **96**, 110405 (2006), cond-mat/0510613.
 - ³⁰ A. Kitaev and J. Preskill, Phys. Rev. Lett. **96**, 110404 (2006), hep-th/0510092.
 - ³¹ D. Poilblanc and G. Misguich, Phys. Rev. B **84**, 214401 (2011), arXiv:1109.5616.
 - ³² Y. Qi, Z.-C. Gu, and H. Yao, (2014), arXiv:1406.6364.
 - ³³ M. P. Zaletel, Y. M. Lu, and A. Vishwanath, to be published.